A Novel Synthesis of Rod-shape BaNiSn-Graphene Decorated TiO 2 Composite as a Ternary Photocatalyst to Improve Visible-Light Driven H 2 Evolution with Lactic acid and TEA

Yonrapach Areerob
King Mongkut's Institute of Technology Ladkrabang
Md Nazmodduha Rafat
Hanseo University
Kefayat Ullah
University of Swat
Won-Chun Oh (wc_oh@hanseo.ac.kr)
Anhui University of Science & Technology

Research Article

Keywords: Rod-shape, Graphene, Co-catalyst, Lactic acid, TEA, H2 evolution

Posted Date: November 21st, 2022

DOI: https://doi.org/10.21203/rs.3.rs-2276116/v1

Abstract

A novel rod-shape BaNiSn-Graphene oxide decorated TiO_2 composite (BaNiSn-GT) has beeen synthesized using a simple ultrasonic method to enhance the visible-light-driven H_2 evolution. The unique structure between the interfaces of BaNiSn-Graphene and TiO_2 provides graphene oxide of contact and excellent electron transfer for H_2 evolution activity. The BaNiSn-GT ternary photocatalyst showed that the BaNiSn-GT displayed the highest H_2-production rate of 1012 μmol h^{-1} g^{-1}, which was about 4 times that of rod-shape BaNiSn and BaNiSn-G under visible light irradiation with scavenger media. Moreover, the higher photocurrent density of BaNiSn-GT is correlated with electron-hole recombination, providing evidence for its inhibition, which leads to a longer lifetime of carriers produced by photoelectrons. The mechanism of the photocatalytic H_2 evolution of BaNiSn-GT based on a full physicochemical characterization was proposed. This study provides new insight into the efficient hydrogen-evolution of graphene-based photocatalysts.

1. Introduction

The evolution of photocatalytic H_2 is an interesting way to generate H_2 and a graphene oxide on way to overcome the threat of an energy crisis. Despite the many efforts that have been devoted to the development of a highly efficient photocatalyst, the practical application of the H_2 evolution rate is still unsatisfactory, this is mainly due to the fast recombination of photogenerated carriers. In one of the newest approaches, heterojunction construction is widely adopted due to its efficiency in facilitating the separation of photogenerated electron-hole pairs and flexibility in material selection [1]. The development of efficient semiconductor composites utilizing visible light for renewable energy production is highly desirable. In many studies to date, many semiconductor materials are used to synthesize photocatalysts that are most suitable and efficient for H_2 production under solar irradiation, such as metal oxides, metal selenides, metal sulfides, metal-organic frameworks, and carbon-based materials commonly used in water photolysis [2–5]. Graphene oxide (GO) has recently attracted considerable attention in the field of energy conversion and environmental improvement due to its distinct advantages such as high conductivity, environmental friendliness, excellent solubility, and chemical inertness [6]. In particular, the formation of band gap energy of graphene oxide can be tuned in a wide energy range by controlling the size or functionality of the energy region, so it can be applied as a semiconductor with narrow gap energy for photocatalytic application.

In addition, it has been reported that the combination of GO and TiO_2 shows improved photocatalytic performance in the field of H_2 evolution and decomposition of pollutants [7, 8]. GO, a photocatalyst in the graphene oxide-TiO_2 heterojunction, generally acts as a photoabsorbent or photo-sensitive agent to maximize photoelectron emission, and acts as an electron acceptor to receive photoelectrons generated from TiO_2 to induce efficient charge separation. However, despite its practical superiority, photocatalytic activity for graphene oxide-TiO_2 binary photocatalysts under visible light irradiation was not significantly

improved for these effects due to the limited ability of graphene oxide to absorb visible light. [9, 10]. To date, many semiconductors with wide visible-light utilization have been explored for hydrogen generation including CdS, ZrO_2, $BaTi_4O_9$, $ZnNb_2O_6$ ternary $ZnIn_2S_4$ materials, and polymer composite. However, their wide application is restricted by many factors, including toxicity, photo-corrosion behavior, and poor photocatalytic efficiency. The construction of a non-toxic, inexpensive, and visible-light responsive photocatalyst for hydrogen evolution remains an urgent and challenging topic. In attempting to overcome these limitations, we try to synthesize multi-component metal sulfide with a tunable band gap and band gap alignment by controlling the composition. Recently, *Mariia* et al. also reports on the integration of $CsPbBr_3$ on g-C_3N_4 nanosheets to construct composite photocatalysts [11]. These works have revealed that a well-designed chemical bonded interface in the heterojunction is beneficial for the photocatalytic process. They found that the chemical bonded interface with extensive areas facilitates the migration of carriers across the junction. Our previous work, BaCuZnS-G-TiO_2 (BCZS-G-T) showed that Ba,and Zn containing compound with graphene oxide has high hydrogen evolution efficiency under visible-light irradiation for H_2 production reaction [12]. For a single conductive or semiconductor material, it is hard to fulfill all demands like cost effective, low bandgap effect and efficient photocatalytic hydrogen evolution. Thus, our study point is to make efficient short-rod type catalyst to for hydrogen evolution [10, 13, 14]. Other issue is implementing graphene oxide with other TiO_2, due to the low band gap of graphene oxide and good catalytic activity of TiO_2. The preparations of graphene oxide based composite nano-composites are convenient and the obtained products are usually more stable than isolated particles. Most importantly, the intimately bonded graphene oxide/TiO_2 surface promotes the separation of the photogenerated electrons and holes, and absorbs a wide range of incident light, thus enhances the photocatalytic performance [15, 16].

In this study, an ultrasonication method was used to synthesize BaNiSn-graphene oxide with a mesoporous TiO_2 (BaNiSn-GT) serving as a co-catalyst for H_2 evolution. We also investigate the photoelectrochemical properties of pure BaNiSn, BaNiSn-G, and BaNiSn-GT, as well as the effects of the most relevant sacrificial hole scavenger on the photocatalytic H_2 evolution performance. Compared to pure BaNiSn and BaNiSn loaded with graphene oxide, the BaNiSn-GT composite exhibits remarkably improved performance in the evolution of photocatalytic H_2. As the loading amount of BaNiSn-graphene oxide with TiO_2 increased, the H_2 generation rate under visible light irradiation ($\theta > 420nm$) increased by about 2.5 times compared to the pure BaNiSn sample. Improved photocatalytic activity can be attributed to the synergistic effect of BaNiSn and graphene oxide-TiO_2, where graphene oxide acts as an electron acceptor and medium, while BaNiSn provides an active site for H_2 production. We hope that this work can contribute to the design and construction of highly efficient visible light-responsive photocatalysts for sustainable energy harvesting and transition.

2. Materials And Methods

2.1. Materials and Regent

Barium chloride ($BaCl_2$, 99.9% trace metals basis), Nickel (II) nitrate hexahydrate ($Ni(NO_3)_2 \cdot 6H_2O$, 94.5-105.5%), and Tin (IV) Chloride Pentahydrate ($SnCl_4 \cdot 5H_2O$, 98%) were purchased from commercial suppliers (Merck, Germany), while Graphene powder was purchased from Sinopharm Chemical Reagent Co., Ltd. (Shanghai, China). Deionized water (DI) was produced using a Direct-Q3 water purification system. All reagents are of analytical grade and used without further purification.

2.2 Synthesis BaNiSn-Graphene-TiO_2 (BaNiSn-GT) photocatalyst

The BaNiSn-GT photocatalyst was synthesized using the ultrasonic method. A three-step combined method was used to synthesize this photocatalyst. First, the BaNiSn (BNS) photocatalyst had to be synthesized. In this preparation, 3.75 g and 4.45 g of Barium chloride (Solution A) and Nickel (II) nitrate hexahydrate (Solution B) were individually dissolved in 50 ml water. Then, the A and B solutions were consistently mixed under vigorous stirring for 1 hour, which we named the AB solution. We took 3.50 g Tin (IV) Chloride Pentahydrate (Solution C) contained in 50 ml Hydrochloric Acid and followed the stirring process for 30 min at 60°C. After that, Solution C was mixed dropwise (2 drops/sec) into the previously prepared AB solution. Then, the solution (ABC solution) was sealed with aluminum foil and stirred overnight at 80°C. Finally, the ultrasonic process was followed for 5 hours with 70 Hz amplitude at 90°C. Then, the precipitation had to be washed several times with DI water and dried at 100°C for 12 hours, followed by calcination at 550°C. This collected sample was named BaNiSn. Empirical results were obtained for the quantification of metal compounds from previous studies [12, 17], and the mixing ratio was determined based on these results. Next, we followed the same process to synthesize BaNiSn-G. To synthesize graphene by the oxidation of graphite powder, we used the Hummer–Offeman's method [18]. First, 15 g of natural graphite and 450 ml of sulfuric acid (H_2SO_4) were mixed with de-ionized water and agitated for an hour at 0°C in an ice bath. Then, the solution was removed from the ice bath, and potassium permanganate (45 g, $KMnO_4$) was slowly added into the solution, which was then continuously agitated at 35°C. After turning to a dim brownish color, the container was sealed and kept at 1°C with agitation for 30 min. Then hydrogen peroxide (H_2O_2) was added dropwise within 5 min. The precipitation was required to wash with acetone and hydrochloric acid (HCl, 10%) several times, and it was heat-treated at 90°C for 12 h until it formed into a graphite oxide powder. At this point, graphite oxide powder was dissolved in 300 mL DI water, agitated for 30 min, and sonicated for 2 h (using Ultrasonic Processor, VCX 750). Finally, the prepared solution was purified and washed with hot water several times. Then, the collected amount of solution was put in an oven for 6 h to obtain graphene oxide powder. The 1.0 g graphene oxide was dissolved in 60 ml of water and 40 ml ethanol, 94.0%, and sonicated for 2 hours. After that, the solution was supposed to be combined with the previously made ABC solution and stirred for 1 hour at 100°C, then sonicated for 5 hours with a 70 Hz amplitude at 90°C. The collected mixture was washed with DI water several times and dried at 160°C for 8 hours. It was then calcinated at 600°C for 3 hours. The collected sample was named BaNiSn-G.

At the final step, 1.8 ml of titanium (IV) isopropoxide, 97.0%, was treated with 4 ml of acetic acid and 30 ml of ethanol, 94.0%. The BaNiSn-G solution was prepared following the same process. Then, the TiO_2 solution was added dropwise into the BaNiSn-G solution and stirred for 1 hour. One more time of sonication was conducted for 3 hours under the same conditions. Then, the precipitation was washed several times and dried at 160°C for 12 hours. Finally, we calcinated the sample at 600°C for 3 hours. The collected sample was names BaNiSn-GT.

2.3 Photocatalytic H_2 production and Scavengers Experiments

In the first step, 50 mg of each of the three types of samples (BaNiSn, BaNiSn-G, and BaNiSn-G) was dispersed in 90 ml of water, and then 10 ml of triethanolamine (TEOA) and an aqueous chloroplatinic acid solution ($H_2PtCl_6 \cdot 6H_2O$, 0.04 g/L) were added. The solution was stirred for 0.5 hours while maintaining a vacuum state. 30 W of LED lamps (Fawoo, Lumidas-H, Korea, $\lambda \geq 420$ nm) were used as a light source, and the reaction system was maintained at 6 ℃ for the entire process. The production of H_2 was determined by the handmade instrumental setting. For hydrogen evolution, we made a handmade set up through U-shape tube with ml/cm scaling. And volume to mol conversion calculation process has been used to calculate the H_2 and O_2 amount. The schematic diagram of the Hydrogen evolution measurement process is shown in Fig. 10. Scavenger's experiments were performed using aqueous solutions containing 0.1 M Na_2SO_4 and one of the following hole scavengers: 20 vol.% methanol (MeOH) (pH = 7), 20 vol.% isopropanol (i-PrOH) (pH = 7), Lactic acid (LA), and Triethanolamine (TEA) were used as a reference under the same conditions.

2.4 Instrumental characterization

The morphology of the samples was examined by Transmission Electron Microscopy (TEM) (JSM5600 JEOL, Japan) (Hitachi HT7700, operated at 100 kV). The crystal structure, binding energy, and chemical composition of the composite sample were performed using X-ray diffraction patterns (XRD, Mini Flex600 diffractometer) and X-ray photoelectron spectroscopy (XPS, K-Alpha, Thermo Fisher Scientific) as AlKa X-ray radiation sources. We used a UV-vis spectrophotometer (SIMADZU UV-2600) to obtain UV-vis diffuse reflectance spectra in the range of 200 to 800 nm. Photoluminescence spectra (PL) were examined using a Fluorescence Spectrophotometer (Hitachi F-7000) with an emission wavelength region of (280–500) nm at RT.

3. Results

3.1 Structural and Surface morphology

The X-ray diffraction (XRD) patterns of BaNiSn, BaNiSn-G, and BaNiSn-GT co-catalyst are displayed in Fig. 1 (a). According to a previous report [19, 20], the graphene exhibits a strong diffraction peak at a 2θ value of 26.3º. The XRD pattern of the BaNiSn sample showed characteristic diffraction peaks of (101),

(510), (110), (004), and (220) at 15.68 º, 22.45º, 23.78 º, 31.78 º, and 34.83 º, respectively. In addition, the peaks were positioned at the angles (2θ) of 25.4◦, 37.9◦, 48.02◦, 53.9◦, and 55.4◦, which correspond to the anatase-phase TiO_2 planes (101), (004), (200), (105), and (211), respectively. The reflective peaks matched with JCPDS No. 48–0928, 15–0780 and 31–0157 corresponding to $BaNiO_2$, $BaSnO_3$ and $BaNiSn_3$ very well, respectively. Furthermore, compared to the XRD pattern of BaNiSn, In the case of the BaNiSn-G sample, some $BaNiO_2$ and $BaSnO_3$ disappeared or showed weak diffraction line peaks, and the $BaNiSn_3$ peak of the metal component was mainly strong. It is believed that some unstable $BaNiO_2$ and $BaSnO_3$ compounds disappeared during the graphene-ultrasonic-hydrothermal reaction. The formation of these crystals showed a similar phenomenon in BaNiSn-GT. In BaNiSn-GT, TiO_2 and $BaNiSn_3$ mainly showed strong peaks. Even in this sample, $BaNiO_2$ and $BaSnO_3$ disappeared or showed weak diffraction line peaks. After loading graphene oxide and TiO_2, these peaks become less pronounced, especially at higher angle, as a result of the reduced diffraction contrast between walls and graphene oxide layer after the incorporation of TiO_2 particles into the layers.

EDX element analysis was performed on the BaNiSn-GT sample. The analysis results for this are shown in (b) and (c) of Fig. 1. From this result, it can be seen that C occupies the largest content. In addition, the content is shown in the order of O and Ba. In addition to these, Ti, Ni, and Sn were additionally found.

Moreover, the surface morphologies of the synthesized BaNiSn, BaNiSn-G, and BaNiSn-GT composites were measured by SEM and TEM images, as shown in Fig. 2 (a-f). Figure 2 (a-c) depicts the overall surface morphologies of BaNiSn, BaNiSn-G, and BaNiSn-GT composites, which were analyzed via SEM investigation. Figure 2 (d-f) shows the morphology of the samples, which presents as rod shaped with highly interconnected regions with transparent outlets, indicating a few nanometers in size rod like structure. Further, after the addition of graphene oxide, multiple layers of graphene flakes were formed in the BaNiSn-G composite. High temperature condition has been used in the synthesis process for the formation of rod like structure. Meanwhile, the interconnected architecture of the BaNiSn-GT showed a larger surface area of TiO_2, which can improve the active size. Figure 2 (d) shows the formation of BaNiSn nanorods with a size of almost 500 nm in aggregated form. Moreover, graphene thin layers could not be clearly observed the BaNiSn surface. Figure 2 (e-f) depicts the TEM image of BaNiSn-GT, which reveals the formation of nanorods that is nicely dispersed on the graphene oxide sheets. The low loading of graphene oxide and TiO_2 can be reasonable for unchanged rod shape structure. The high temperature treatment produced framework shrinkage and the samples-maintained rod like structure.

3.2 Chemical composition

By analyzing X-ray photoelectron spectroscopy (XPS), the interfacial interaction among BaNiSn, graphene oxide, and TiO_2 compounds was studied, and the surface composition and chemical state of BaNiSn-GT were analyzed as shown in Fig. 3 (a-f). Figure 3 (a) shows high-resolution XPS spectrum irradiation of Ba3d, Ni2p, Sn3d, O1s, C1s, and Ti2p. The main peak of Ni2p is divided into six sub-peaks by deconvolution operation [21]. Two spin split peaks located at 853.3 and 870.2 eV demonstrate the

presence of Ni^{2+}. Furthermore, the double peaks located at 861.4 and 879.6 eV imply the presence of corresponding satellite peaks ($Ni2p_{3/2}$ and $Ni2p_{1/2}$) (Fig. 3 (b)). Peaks of 780.3 and 795.6 eV having a division value of 15.3 eV are all assigned to Ba^{2+} (Fig. 3 (c)) Also, in Fig. 3 (d), peaks at 486.8 and 495.4 eV are all assigned to Sn^{4+}. Figure 3 (e) shows two binding energy peaks of C1s at 285.5 and 289.5 eV confirming C = C and C = O or O-C = C, respectively. As can be seen from Fig. 3 (f), the Ti^{4+}-O bond of the TiO_2 lattice is typical of the photoelectron peaks of $Ti2p_{3/2}$ and $Ti2p_{1/2}$ around 458.7 and 464.4 eV, respectively [22–24]. The results can confirm the structure of the BaNiSn-GT composite. In the overall XPS survey results, the intensity of the peak was significantly different, and the quantitative relationship of the element can be seen from this intensity. The intensity of C1s was the largest, and after that, the intensity of the peak gradually decreases in the order of O1s and Ni2p. Also, it can be found that Ti2p, Ba3d, and Sn3d show small peak intensity and occupy a small amount quantitatively. The peaks of O1s consisted of four peaks mainly occurring at 530.50 eV of O-Me, 532.55 eV of O = C, 533.95 eV of O–C = O, and 540.50 eV of O–OH (Fig. 3 (g)).

3.3 Raman Analysis

Spectra of BaNiSn, BaNiSn-G and BaNiSn-GT measured by Raman spectroscopy are shown in 4, and the main Raman shift peaks at 394 cm^{-1} (B_{1g}), 517 cm^{-1} (A_{1g}), and 638 cm^{-1} (E_g) are due to the characteristic peaks of titanium dioxide nanotubes [25]. The two weak peaks at positions 1350 and 1600 cm^{-1} are due to the D-band and G-band derived from graphene, respectively. According to graphene's double resonance theory, 1387 cm^{-1} with a high D-band frequency results from disturbance of the connected hexagonal ring base plane [17]. In addition, the general E_{12g} and A_{1g} vibration modes of BaNiSn showed active modes of 425 and 3425 cm^{-1}, respectively, which is believed to be due to metal compounds. In our experiments, the blue shift of D-band and G-band (approximately 30 cm^{-1}) is likely due to the combined action of quantum confinement effects and the strong interaction between the three compounds of BaNiSn, TiO_2 and GO.

3.4 Optical performance

Light absorbance spectroscopy has been analyzed to confirm the light response of the samples. From the Fig. 5a, it is apparent that the pure BaNiSn has less light absorption ability. After implemented the graphene oxide and TiO_2, light response increased. Thus BaNiSn-G, BaNiSn-GT have shown stable peak in the more visible light region. Furthermore, to study the optical absorbances of the BaNiSn, BaNiSn-G, and BaNiSn-GT composites, ultraviolet-visible diffuse reflectance spectroscopy was conducted (Fig. 5b). The bandgaps of the samples were evaluated by the Kubelkae-Munk function [17]

$$\alpha h\nu = C_1 (h\nu - Eg)^{1/2} \quad (1)$$

Where α, h, ν, Eg, and C_1 are absorption coefficients, plank constants, optical frequencies, bandgap energy, and constants, respectively. Reflectivity was converted into absorbance data, and for this transformation, the Kubelkaie-Munk theory was used to obtain it. The photoabsorption increased significantly in the

range of 2.3 to 1.1 eV. Pure BaNiSn showed 2.05 eV, and the BaNiSn-GT composite presents a band gap of 1.10 eV, which was lower than pure BaNiSn. Low band gap energy values are advantageous for the production of H_2 evolution under visible light irradiation.

3.5 Possible photocatalytic mechanisms (Mott-Schottky plots)

Theoretical analysis and experimental tests were used simultaneously to verify the successful formation of the Z-system in the composite heterojunction structure. Figure 6 shows a Mott-Shotky plot of BaNiSn, BaNiSn-G, and BaNiSn-GT using a saturated calomel electrode as a reference electrode, and may measure a flat band potential of a material from the plot. In the n-type semiconductor, the flat band potential may be approximated by the position of the energy region of the conductive band CB. From the measured results, the CBs of BaNiSn, BaNiSn-G and BaNiSn-GT are located at -0.6, -0.42, -0.31 V (vs NHE, pH = 7), respectively. Based on the band gap data obtained from the UV-Vis diffusion reflectance spectrum, the valence band positions (VB) of GO and TiO_2 are located at + 2.4 and + 3.2V, respectively.

3.6 Photonic spectroscopic analysis (PL, EIS spectra, and Photocurrent)

Close interface contact between Junction bonded semiconductors is advantageous for the separation of electrons and holes produced by irradiated light that can be determined by photo-electrochemical measurements. The PL spectrum is described as some combination of photoelectrons and holes received by the semiconductor. The higher the PL strength of the photocatalytic semiconductor composite compound, the slower the recombination and the shorter the electron lifetime. Figure 7(a) shows PL spectra of TiO_2, GO, BaNiSn, BaNiSn-G, and BaNiSn-G at an excited wavelength of 550 nm. The emission peak of the BaNiSn-G shows strength similar to that of BaNiSn-GT in the range of 450 to 650 nm. However, BaNiSn-GT showed the lowest peak intensity, and the PL intensity of BaNiSn showed the strongest curve. When BaNiSn-GT was incorporated, the PL strength of BaNiSn decreased dramatically, suggesting a longer lifetime of photo-generated electron-hole pairs [26]. As is well known, TiO_2 and GO are basic substances. The results of PL analysis on these can be seen from many documents [12, 27]. Our previous work [12] shows that TiO_2 exhibits a high PL curve due to the large bandgap energy value. This shows the effect of the photo-reaction effect late due to the late electron transfer reaction. However, the graphene complex compound presented in this study shows a low PL curve because the electron transfer reaction proceeds easily and quickly.

Junction-bonded composites have been studied by electrochemical impedance spectroscopy (EIS). From the Nyquist plot (Fig. 7(b)) it can be clearly observed that the circle radius of BaNiSn-GT is small in the BaNiSn and BaNiSn-G samples, indicating an increase in conductivity and improved charge separation ability after addition of graphene oxide. These results further confirm the higher efficiency of the BaNiSn-GT composite, as shown by photocurrent and photocatalytic experiments, which exhibit the smallest electron transfer resistance at the semiconductor/electrolyte interface. GO is a good conductive material

in complex compound studies [12, 28, 29]. When the metal compound forms a complex with GO, the metallic complex has good photo-electron transfer effect due to the synergy effect. In the results of previous studies [29], many results can be seen. As shown in Fig. 7(b), the GO composite shows the effect of improving the conductivity.

The photocurrent density of the composite is the key to enhancing the performance of the photocatalyst. The instantaneous transient photocurrent measurement of BaNiSn-GT under visible light irradiation is shown in Fig. 7(c). A higher photocurrent value corresponds to a higher photogenerative charge density, resulting in a more necessary charge for the photooxidation-reduction reaction at the BaNiSn-GT heterojunction. BaNiSn-GT obtained the strongest reaction value of 13800 μA cm^{-2}. After four cycles of intermittent on/off irradiation, the stability of the graphene oxide rod photoelectric response of BaNiSn-GT was demonstrated through a nearly decay-free photocurrent curve.

3.6 H_2 evolution analysis and Scavenger Effect

The activity of the prepared photocatalyst for hydrogen production was conducted under visible light irradiation for 4 hours and was investigated in the presence of visible light of the aqueous methanol solution as a sacrificial agent. These results are shown in Fig. 8 (a), which shows that BaNiSn-GT exhibits relatively high photocatalytic activity with a hydrogen evolution rate of 1012 μmol/h. On the other hand, BaNiSn-G and BaNiSn composites exhibited significantly lower hydrogen evolution rates of 910 μmol/h and 835 μmol/h. The beneficial effect of the complex photocatalyst is the combination of wide band gap and narrow band gap semiconductors, which can significantly improve the interface reaction speed due to the expansion of the life of the charge carrier. In addition, this combination leads to the result of photocatalysts with improved absorption efficiency in the range of visible light by solar irradiation.

Radical capture experiments using complex photocatalysts and scavengers were also conducted. Na_2SO_4, methanol, ethanol, lactic acid (LA), and triethanolamine (TEA) were adopted as scavengers, respectively. As shown in Fig. 8 (b), the addition of TEA has the highest effect on the degradation efficiency, whereas the addition of Na_2SO_4, methanol, and ethanol having the same concentration and volume leads to almost 50% inhibition effect of the degradation efficiency. Thus, h^+ and •OH are essential for the evolution of photocatalytic hydrogen, and in this reaction, •OH has a greater effect than h^+. Also, as shown in Fig. 9, the VB position of TiO_2 is much closer to the CB position of BaNiSn-G at the hetero interface. The distance between VB and CB position reduced due to zero band gao of graphene oxide. Addition of graphene oxide and TiO_2 produced a mid bandgap and hinder the recombination (electron to hole conversion). Thus, the electron lifetime increase and enhance the photocatalytic activity. During light excitation, the photoinduced electrons on the CB of BaNiSn-G can be spatially described as their movement between CB and VB to create a photo-generating hole on the VB. This is an irrefutable solid Z-system charge transfer process over heterogeneous interfaces. The role of BaNiSn in this photoelectron transfer reaction is high hydrogen production by controlling band gap energy. In the photocatalytic experiment, BaNiSn produced an oxide radical to produce a metal-electron conversion. Hydrogen

molecules can be dissociated through adsorption on the surface of the metal catalyst. In the next step, the hydrogen atom moves from the metal catalyst to the non-metal support or adsorbent. Here, the sacrificial scavenger acted as an electron donor that played an intermediate role. In the experiment, the sacrificial scavenger released electrons, which, as shown in Fig. 9, atoms covered holes in the band and increased hole-electron conversion, which is an active site for efficient photocatalytic activity of the photocatalyst. The addition of an auxiliary sacrificial agent also increases the amount of hydrogen evolution.

Table 1
Some examples for H_2 evolution amounts with other catalysts

Catalyst	H_2 evolution amounts (with the scavenger)	H_2 evolution amounts	References
CoMoSx		3.85 μmol/g for 1 min	30
FeMoSx		1.57 μmol/g for 1 min	30
NiMoSx		4.93 μmol/g for 1 min	31
BaCuZnS-graphene- TiO_2	5541.04 μmol/g/4 h	2715.60 μmol/g for 4 h	12
LaCdSe-GO- TiO_2	443.28 μmol/g.	324.15μmol/g for 4h (sonophotocatalytic)	32
ZnS:Eu quantum dots	11100 μmol/g/h	9000 μmol/g for 1h	33
$Ni_6(SCH_2Ph)_{12}$-TiO_2		5600 μmol/g for 1h	34
WSe_2-graphene-TiO_2	2.004 mmol/ 11 h	1.718 mmol/g for 11 h	35

The results of previous studies on hydrogen production studies with several types of photocatalysts are shown in Table 1. Since they have different research conditions such as reaction time and the presence or absence of scavengers, quantitative comparison is problematic. However, from these studies, the accessibility of reactor design and commercialization can be considered in the future.

4. Conclusions

In summary, the unique structure of the BaNiSn-GT co-catalyst was successfully prepared using an ultrasonic method. Photoelectrochemical measurements proved that BaNiSn, graphene oxide, and TiO_2 act as photo-sensitive agents to react to visible light reactions. The Junction-bonded BaNiSn-GT complex exhibits enhanced photocatalytic H_2 production activity and stability under visible light irradiation due to the combination of extended visible light absorption capacity, long life of photogenerated electron-hole

pairs, and fast interfacial charge transfer rates. The ability of the selected sacrificial agent to clean the photogenic holes was evident in the order of Na_2SO_4, methanol, ethanol, LA, and TEA solutions. The presence of the sacrificial agent also results in a negative change in the starting potential of the photocurrent, which can be largely explained by the different redox potentials of the additive. This work not only provides an innovative strategy for synthesizing heterojunction ternary hybrid nanocomposites, but also provides new insights to understand the essential role of BaNiSn and TiO_2 in graphene oxide-based nanohybrids.

Declarations

Conflicts of Interest:

Declare conflicts of interest or state “The authors declare no conflict of interest.” Authors must identify and declare any personal circumstances or interest that may be perceived as inappropriately influencing the representation or interpretation of reported research results. Any role of the funders in the design of the study; in the collection, analyses or interpretation of data; in the writing of the manuscript; or in the decision to publish the results must be declared in this section. If there is no role, please state “The funders had no role in the design of the study; in the collection, analyses, or interpretation of data; in the writing of the manuscript; or in the decision to publish the results”.

References

1. Dong Y., Hu Q., Li B., Li X., Chen M., Zhang M., Feng Y., Ding Y., Aminated silicon dioxide enriching iron-containing polyoxometalate catalyst confined in CdS for efficient H_2 evolution, Applied Catalysis B: Environmental, 2022, 304, 120998.
2. Zhou H., Chen R., Han C., Wang P., Tong Z., Tan B., Huang Y., Liu Z., Copper phosphide decorated g-C_3N_4 catalysts for highly efficient photocatalytic H_2 evolution, Journal of Colloid and Interface Science, 2022, 610, 126-135.
3. Li X., Hu J., Yang T., Yang X., Qu J., Li C., Efficient photocatalytic H_2-evolution coupled with valuable furfural-production on exquisite 2D/2D $LaVO_4$/g-C_3N_4 heterostructure, Nano Energy, 2022 , 92, 106714.
4. Cao B., Wan S., Wang Y., Guo H., Ou M., Zhong Q., Highly efficient visible-light-driven photocatalytic H_2 evolution integrated with microplastic degradation over MXene/ZnxCd1-xS photocatalyst, Journal of Colloid and Interface Science, 2022, 605, 311-319.
5. Cao H., Zhang D., Ning X., Geng J., Constructing magnetically recoverable CdS/$CaFe_2O_4$ P–N heterojunctions for enhanced photoelectrochemical properties towards H_2 evolution reaction, Ceramics International, 2021, 47, 14, 19668-19677.
6. Choi J.S., Park H.B., Yoon O.J., Kim H.J, Investigation on the role of graphene oxide sheet-platinum composite counter electrode in dye-sensitized solar cell, Thin Solid Films, 2022, 745, 139098.

7. Wang P., Deng P., Cao Y., Edge-sulfonated graphene-decorated TiO_2 photocatalyst with high H_2-evolution performance, International Journal of Hydrogen Energy, 2022, 47, 2, 1006-1015.
8. Altin I., CuO-TiO_2/graphene ternary nanocomposite for highly efficient visible-light-driven photocatalytic degradation of bisphenol A, Journal of Molecular Structure, 2022, 1252, 132199.
9. Lv X., Zhang G., Fu W., Highly Efficient Hydrogen Evolution Using TiO_2/Graphene Composite Photocatalysts, Procedia Engineering, 2012, 27, 570-576.
10. Gong, W., Meng, X., Tang, X. and Ji, P., 2017. Core-shell MnO_2-SiO_2 nanorods for catalyzing the removal of dyes from water. Catalysts, 7(1), p.19.
11. Pavliuk M.V., Abdellah M., Sá J., Hydrogen evolution with $_{CsPbBr3}$ perovskite nanocrystals under visible light in solution, Materials Today Communications, 2018, 16, 90-96,
12. Rafat, M.N., Cho, K.Y., Jung, C.H. and Oh, W.C., 2020, New modeling of 3D quaternary type BaCuZnS-graphene-TiO_2 (BCZS-GT) composite for photosonocatalytic hydrogen evolution with scavenger effect. Photochemical & Photobiological Sciences, 19(12), pp.1765-1775.
13. Chen, H., Chen, Z., Yang, H., Wen, L., Yi, Z., Zhou, Z., Dai, B., Zhang, J., Wu, X. and Wu, P., Multi-mode surface plasmon resonance absorber based on dart-type single-layer graphene. *RSC advances*, 2022, *12*(13), 7821-7829.
14. Zhang, Z., Cai, R., Long, F. and Wang, J., Development and application of tetrabromobisphenol A imprinted electrochemical sensor based on graphene/carbon nanotubes three-dimensional nanocomposites modified carbon electrode. *Talanta*, 2015, *134*, pp.435-442.
15. Zaaba, N.I., Foo, K.L., Hashim, U., Tan, S.J., Liu, W.W. and Voon, C.H., 2017. Synthesis of graphene oxide using modified hummers method: solvent influence. Procedia engineering, 2017, 184, pp.469-477.
16. Shangguan, Q., Chen, Z., Yang, H., Cheng, S., Yang, W., Yi, Z., Wu, X., Wang, S., Yi, Y. and Wu, P., Design of ultra-narrow band graphene refractive index sensor. Sensors, 2022, 22(17), p.6483.
17. Eskandari M., Shahbazi N., Marcos A.V., Malekfar R., Taboada P., Facile MOF-derived $NiCo_2O_4$/r-GRAPHENE OXIDE nanocomposites for electrochemical energy storage applications, Journal of Molecular Liquids, 2022, 348, 118428.
18. Wang X., Liu X., Liu X., Su Y., Wang J., Fan T., Ning X., Seeram Ramakrishn, Yun-Ze Long, Ultralight and multifunctional PVDF/SiO_2@GRAPHENE OXIDE nanofibrous aerogel for efficient harsh environmental oil-water separation and crude oil absorption, Carbon, 2022, 193, 77-87.
19. Zhang J., Jia X., Liu T., Yang J., Wang S., Li Y., Shao D., Feng L., Song H., Facile strategy to synthesize porous GRAPHENE OXIDE/ZnO heterostructure for enhanced acetone gas sensing properties, Sensors and Actuators B: Chemical, 2022, 359, 131601.
20. Zhang C., Guo H., Gao Y., Graphene oxideng Y., Jin C., He J., Controllable synthesis of Co_3W_3N supporting on N-doped GRAPHENE OXIDE as electrocatalysts for oxygen reduction reaction, Chemical Physics Letters, 2022, 793, 139429,

21. Wang Y., Li J., Yuan R., Gao H., Lv J., Xue D., Hao X., Yang Y., Lookman T., Dkhil B., Lou X., Enhanced electrocaloric effect in BaSn/TiO_3 ceramics by addition of CuO, Journal of Alloys and Compounds, 2021, 851, 2021, 156772.
22. Guechi A., Chegaar M., Bouhemadou A., Electronic and optical properties of polar intermetallic compound $BaSn_3$: First principles study, Optik, 2020, 219, 165028,
23. Chen D., Yu W., Wei L., Ni J., Li H, Chen Y., Tian Y., Yan S., Mei L., Jiao J., High sensitive room temperature NO_2 gas sensor based on the avalanche breakdown induced by Schottky junction in TiO_2-Sn_3O_4 nanoheterojunctions, Journal of Alloys and Compounds, 2022, 912, 165079.
24. Sugikumar M.V., Sakthivel V.V., Mandarasalam G., Kalayanasundram M., Subramanian S., Photocatalytic degradation of phenylene diamine using TiO_2-rGRAPHENE OXIDE under UV radiation, Materials Today: Proceedings, 2022, 57, Part 4, 1694-1699.
25. Wahyuningsih S., Ramelan A.H., Pramono E., Nuryana H.P., Mujahidin M.M.A., Munawaroh H., Hidayat R., Fadillah G., Transformation growth of nanoflower-like GRAPHENE OXIDE-ZnO as an active site platform for H_2S sensors, Chemical Physics Letters, 2022, 790, 139351.
26. Zhou H., Chen R., Han C., Wang P., Tong Z., Tan B., Huang Y., Liu Z., Copper phosphide decorated g-C_3N_4 catalysts for highly efficient photocatalytic H_2 evolution, Journal of Colloid and Interface Science, 2022, 610, 126-135.
27. Thao, L.T.S., Dang, T.T.T., Khanitchaidecha, W., Channei, D. and Nakaruk, A., Photocatalytic degradation of organic dye under UV-A irradiation using TiO_2-vetiver multifunctional nano particles. *Materials*, 2017, *10*(2), p.122.
28. Hsu, C.P., Lee, K.M., Huang, J.T.W., Lin, C.Y., Lee, C.H., Wang, L.P., Tsai, S.Y. and Ho, K.C., EIS analysis on low temperature fabrication of TiO2 porous films for dye-sensitized solar cells. Electrochimica Acta, 2008, 53(25), pp.7514-7522.
29. Liu Q., Shi Q., Wang H., and Zhang Q., Laser irradiated self-supporting and flexible 3-dimentional graphene-based film electrode with promising electrochemical properties, RSC Advances 2015, 5, 58, DOI:10.1039/C5RA08431H
30. Fu, G.; Lee, J. M. Ternary metal sulfides for electrocatalytic energy conversion. *Journal of Materials Chemistry A*, **2019**, 7(16): 9386-9405.
31. Wang, W.; Yang, L.; Qu, F.; Liu, Z.; Du, G.; Asiri, A. M . A self-supported $NiMoS_4$ nanoarray as an efficient 3D cathode for the alkaline hydrogen evolution reaction. *Journal of Materials Chemistry A*, **2017**, 5(32): 16585-16589.
32. Kovtun A, Jones D, Dell'Elce S, Treossi E, Liscio A, Palermo V. Accurate chemical analysis of graphene-based materials using X-ray photoelectron spectroscopy. Carbon, 2019, 143: 268-275
33. Poornaprakash, B.; Vattikuti, S. P.; Subramanyam, K.; Cheruku, R.; Devarayapalli, K.; Kim, Y. L.; Park, H.; Reddy, M. S. P. Photoluminescence and hydrogen evolution properties of ZnS: Eu quantum dots. *Ceramics International*, **2021**, 47(20): 28976-28984.

34. Tian, F.; Chen, J.; Chen, F.; Liu, Y.; Chen, R. Boosting hydrogen evolution over $Ni_6(SCH_2Ph)_{12}$ nanocluster modified TiO_2 via pseudo-Z-scheme interfacial charge transfer. Applied Catalysis B: Environmental, 2021, 292: 120158.
35. Zhu, L.; Nguyen, D. C. T.; Woo, J-H; Zhang, Q. F.; Cho, K. Y.; Oh, W. C. An eco-friendly synthesized mesoporous-silica particle combined with WSe_2-graphene- TiO_2 by self-assembled method for photocatalytic dye decomposition and hydrogen production. *Scientific reports*, **2018**, 8(1): 1-14.

Scheme

Scheme 1 is available in Supplementary Files section.

Figures

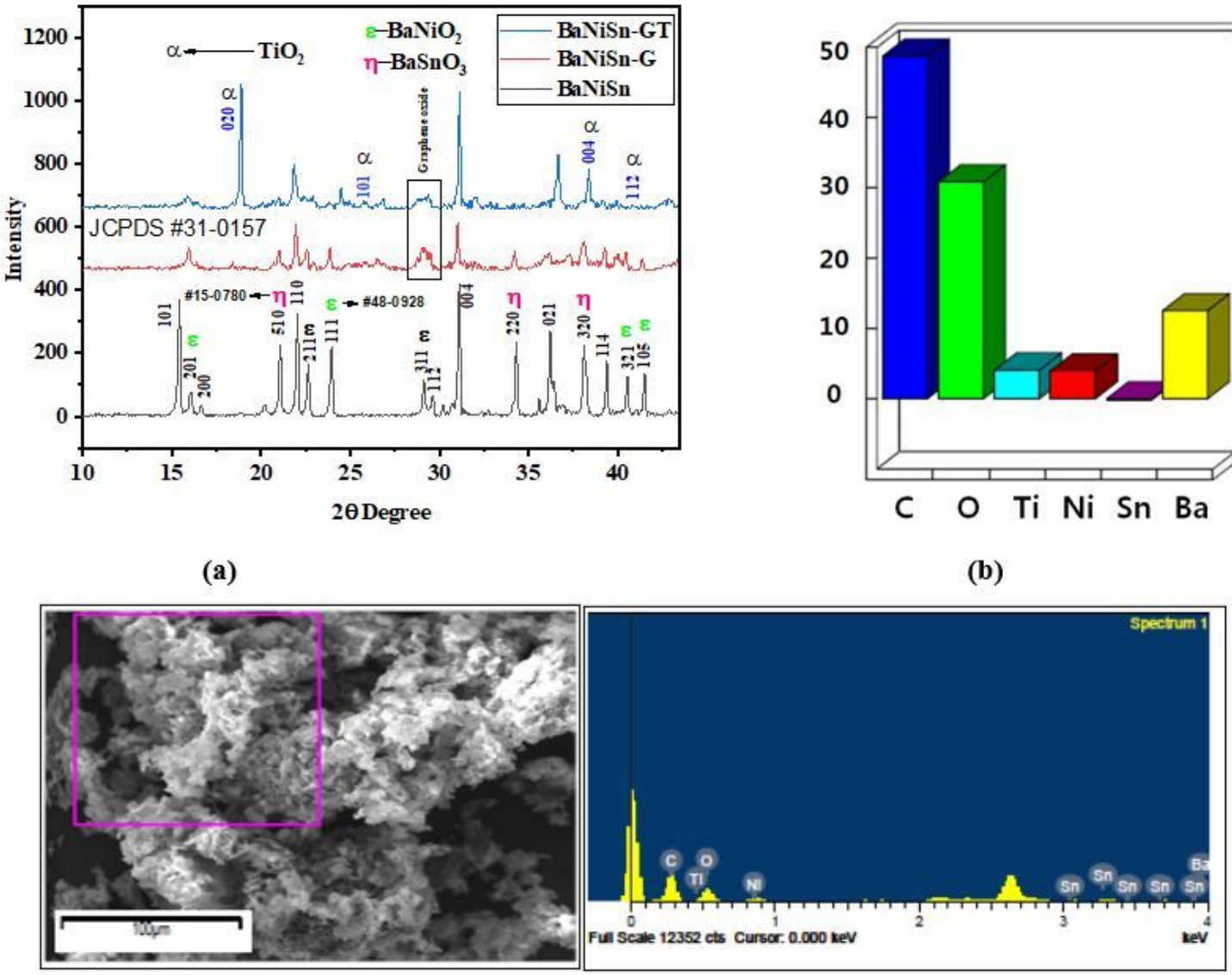

Figure 1

Crystal structure and elemental analysis; **(a)** XRD patterns of BaNiSn, BaNiSn-G and BaNiSn-GT, **(b)** and **(c)** EDX analysis of BaNiSn-GT.

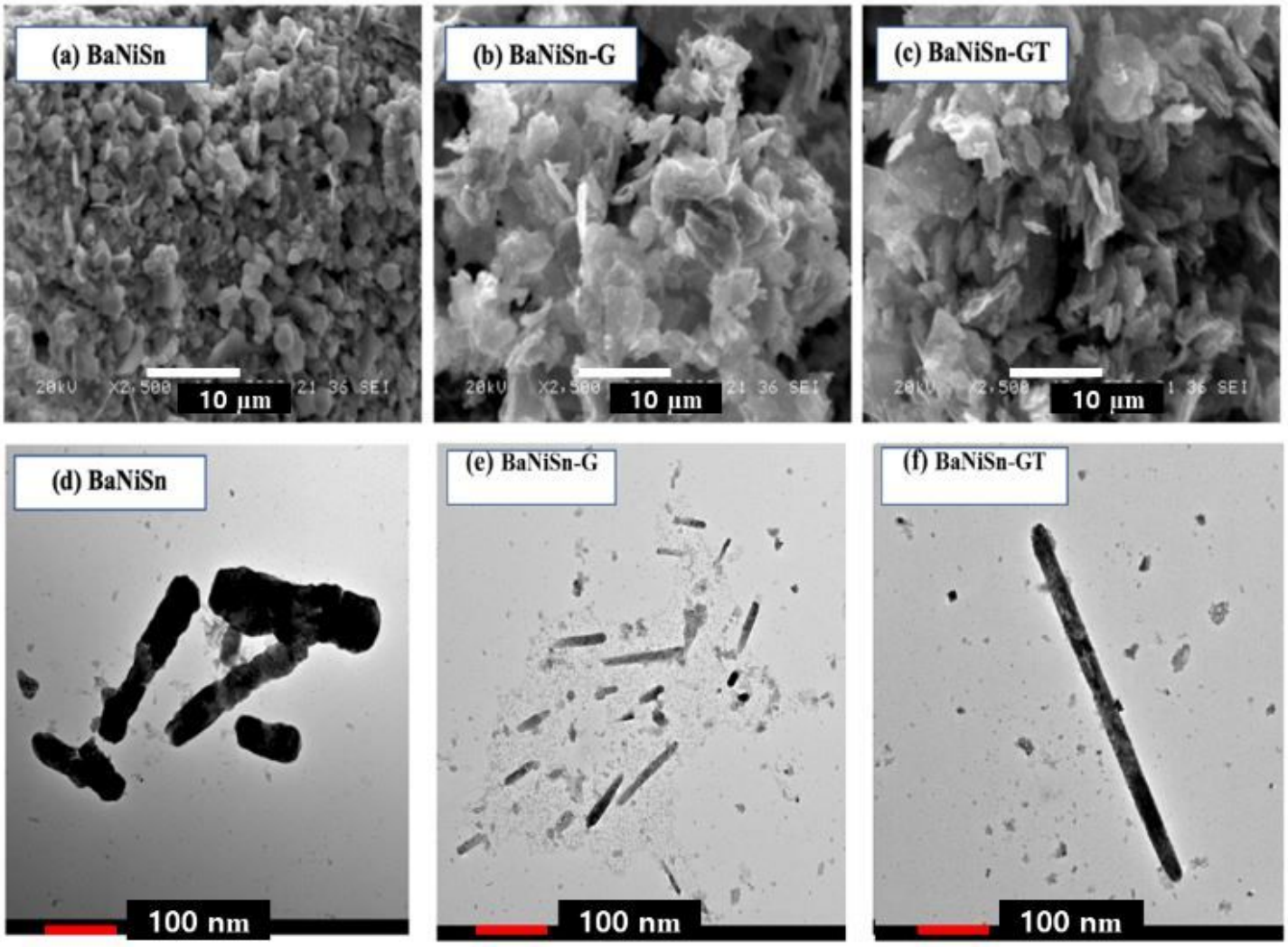

Figure 2

SEM and TEM images of (a, d) BaNiSn, (b, e) BaNiSn-G and (c, f) BaNiSn-GT.

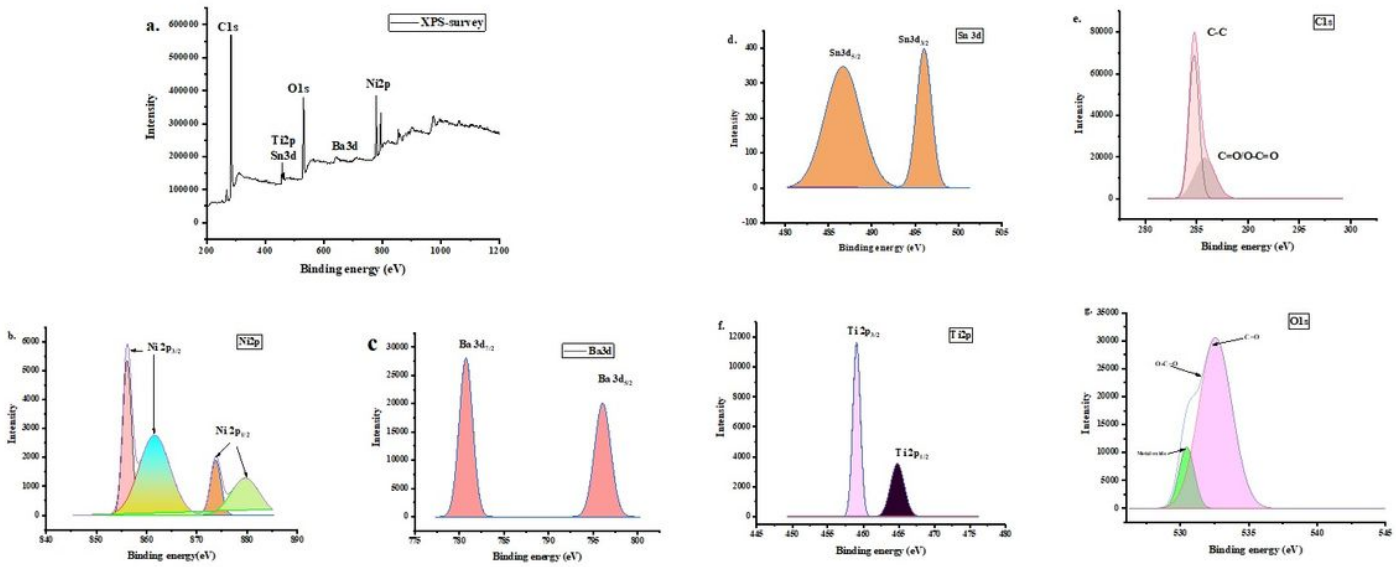

Figure 3

XPS spectra (a) full XPS survey, (b) Ni 2p, (c) Ba 3d, (d) Sn 3d, (e) C1s, (f) Ti 2p and (g) O1s.

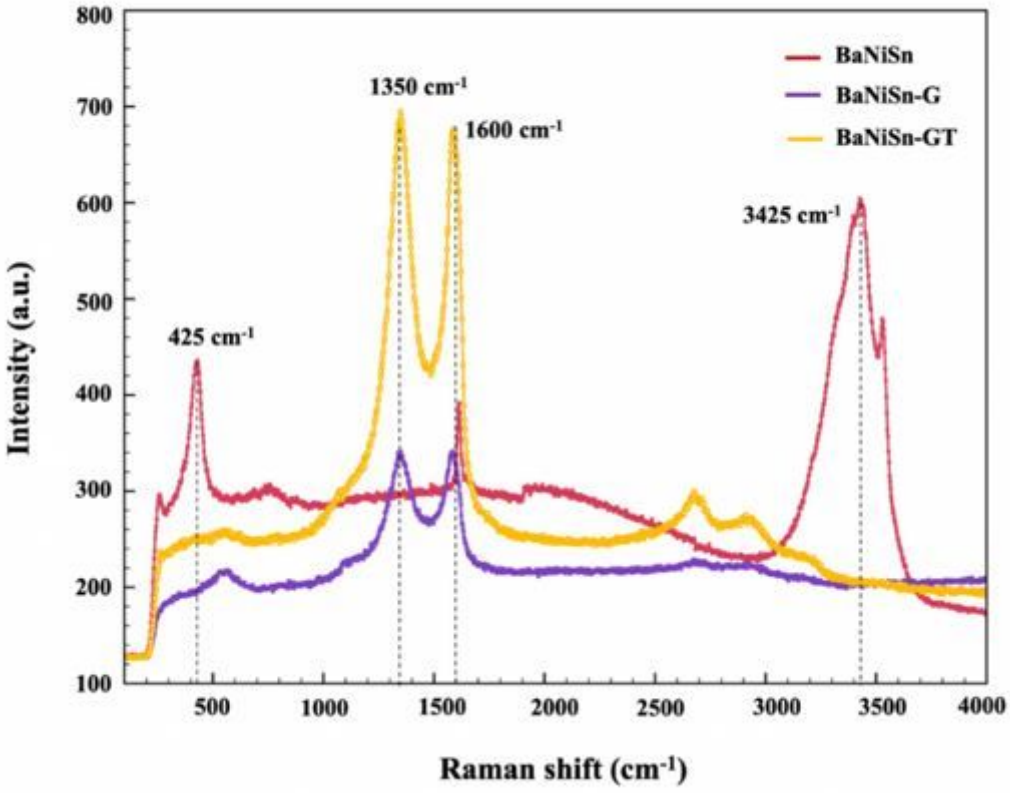

Figure 4

Raman Spectra of BaNiSn, BaNiSn-G and BaNiSn-GT.

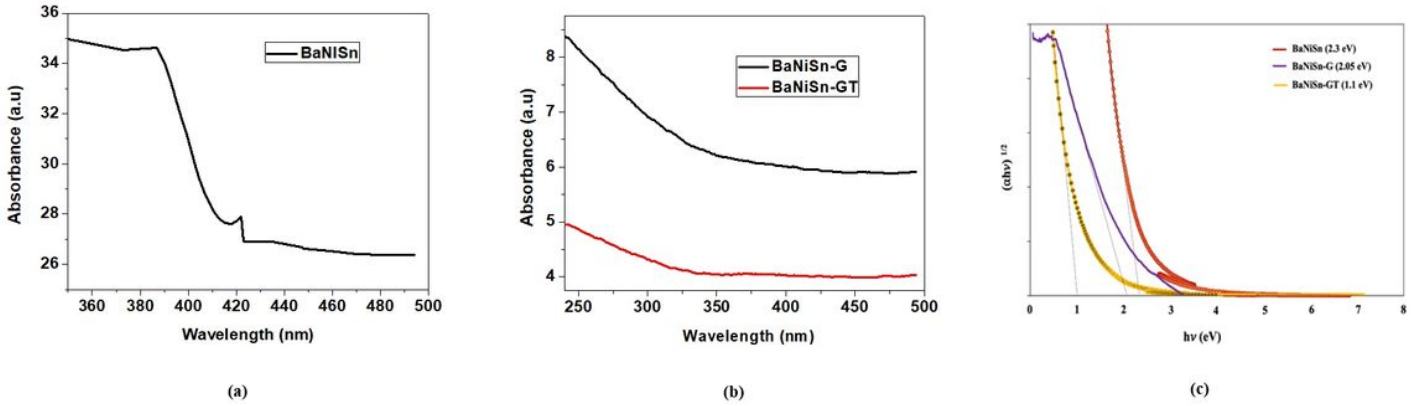

Figure 5

UV-Vis DRS spectra (a) light absorption spectrum of BaNiSn, (b) light absorption spectra of BaNiSn-G and BaNiSn-GT and (c) the bandgap energy of BaNiSn, BaNiSn-G and BaNiSn-GT corresponding Kubelkae-Munk function spectra.

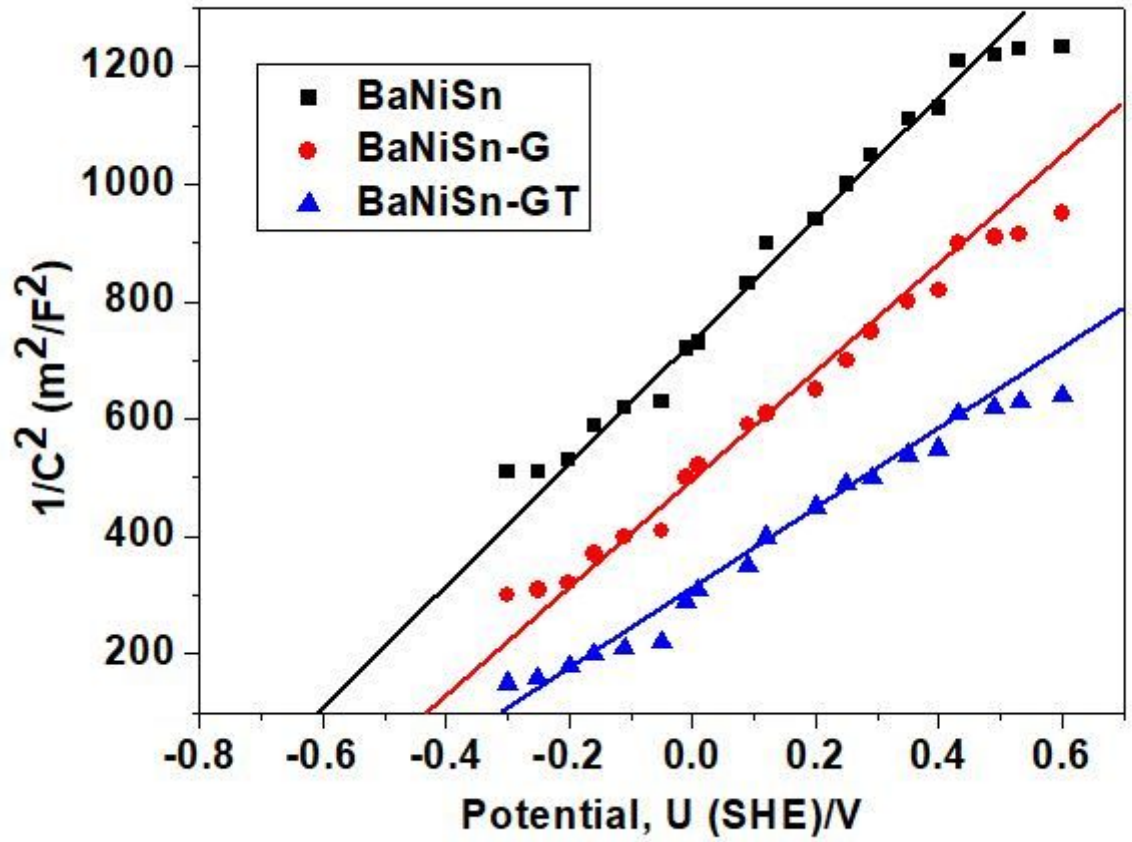

Figure 6

Mott-Schottky analysis for calculation of donor density and flat band potential.

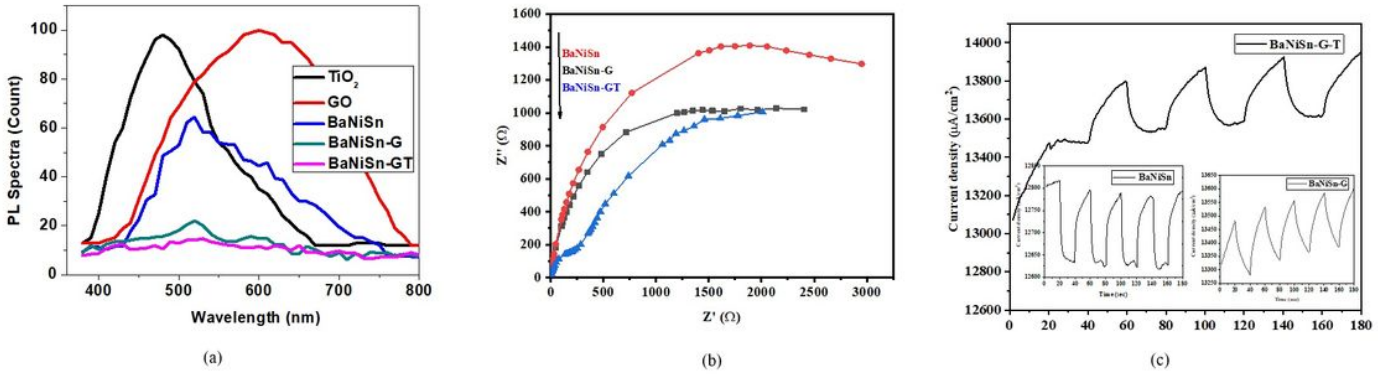

Figure 7

Photonic spectroscopic analysis (a) PL Spectra, (b) EIS Spectra and (c) Photocurrent density of BaNiSn, BaNiSn-G and BaNiSn-GT.

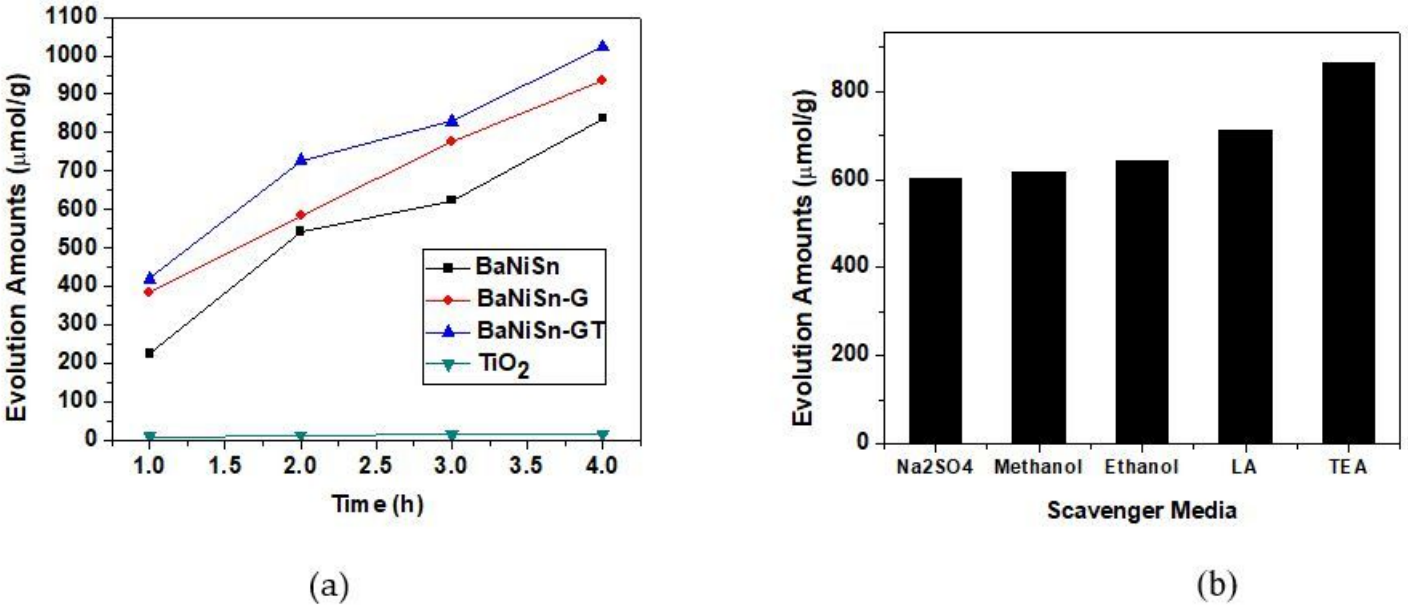

Figure 8

Hydrogen evolution amounts ; (a) TiO_2, BaNiSn, BaNiSn-G and BaNiSn-GT photocatalysts under visible light and (b) BaNiSn-GT photocatalyst under visible light and scavenger media (LA; Lactic acid and TEA; Triethanolamine) during 1 hour.

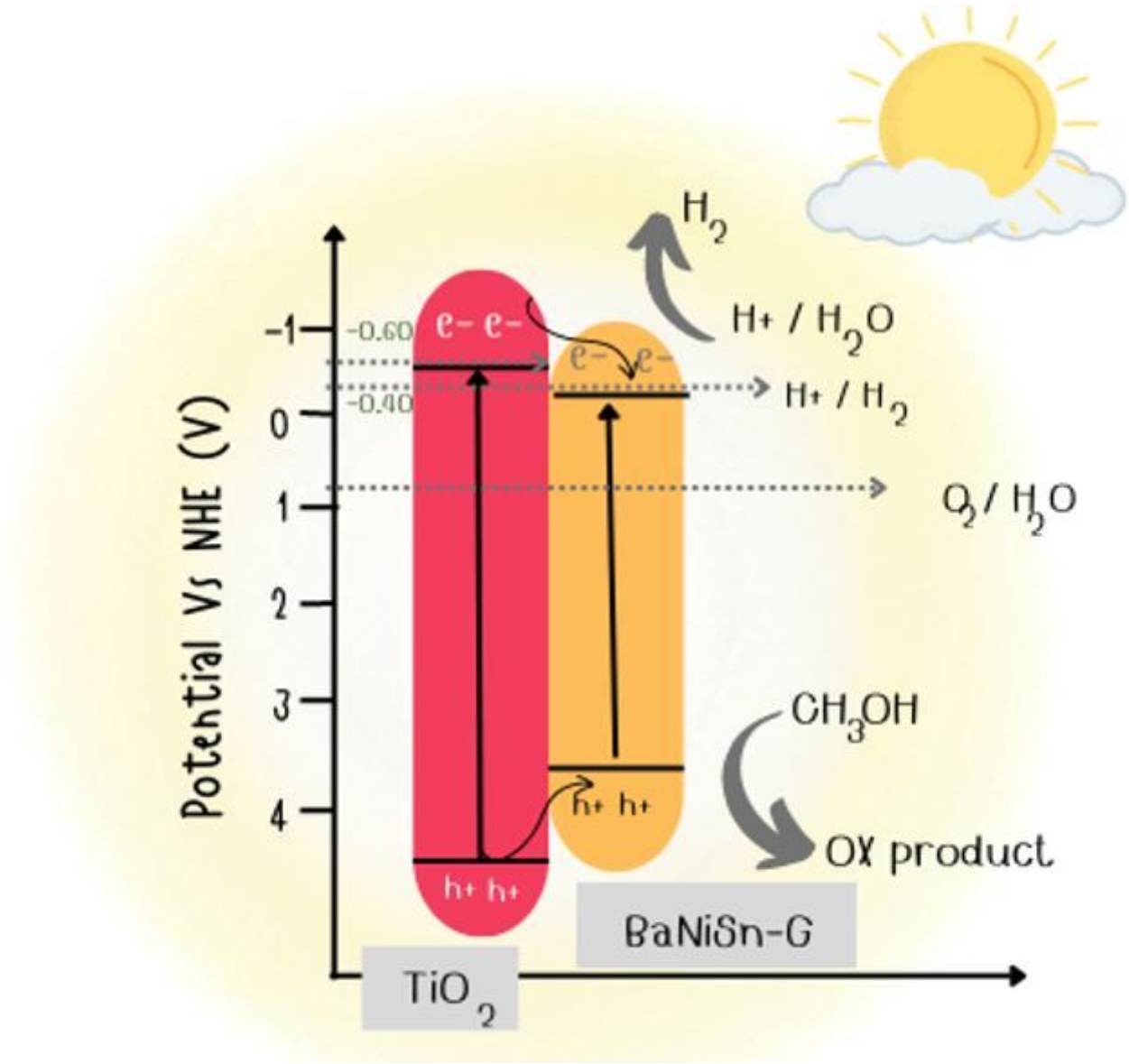

Figure 9

Schematic diagram showing the energy band structure and electrons transfer in the BaNiSn-GT heterojunction.

Supplementary Files

This is a list of supplementary files associated with this preprint. Click to download.

- Scheme1.jpg